

# Electronic Modulation of Pt Nanoparticles on Ni<sub>3</sub>N–Mo<sub>2</sub>C by Support-Induced Strategy for Accelerating Hydrogen Oxidation and Evolution

Yuting Yang, Qiumei Dai, Luyan Shi, Yi Liu, Tayirjan Taylor Isimjan,\* and Xiulin Yang\*



Cite This: *J. Phys. Chem. Lett.* 2022, 13, 2107–2116



Read Online

ACCESS |



Metrics & More

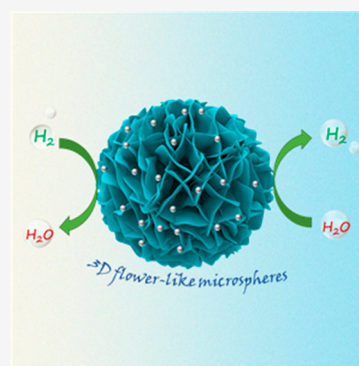


Article Recommendations



Supporting Information

**ABSTRACT:** Electrochemical energy conversion and storage through hydrogen has revolutionized sustainable energy systems using fuel cells and electrolyzers. Regrettably, the sluggish alkaline hydrogen oxidation reaction (HOR) hampers advances in fuel cells. Herein, we report a Pt/Ni<sub>3</sub>N–Mo<sub>2</sub>C bifunctional electrocatalyst toward HOR and hydrogen evolution reaction (HER). The Pt/Ni<sub>3</sub>N–Mo<sub>2</sub>C exhibits remarkable HOR/HER performance in alkaline media. The mass activity at 50 mV and exchange current density of HOR are 5.1 and 1.5 times that of commercial Pt/C, respectively. Moreover, it possesses an impressive HER activity with an overpotential of 11 mV @ 10 mA cm<sup>-2</sup>, which is lower than that of Pt/C and most reported electrocatalysts under the same conditions. Density functional theory (DFT) calculations combined with experimental results reveal that Pt/Ni<sub>3</sub>N–Mo<sub>2</sub>C not only possesses an optimal balance between hydrogen binding energy (HBE) and OH<sup>-</sup> adsorption but also facilitates water adsorption and dissociation on the catalyst surface, which contribute to the excellent HOR/HER performance. Thus, this work may guide bifunctional HOR/HER catalyst design in the conversion and transport of energy.



As an attractive and clean energy carrier, hydrogen has been regarded as the most promising substitute for traditional fossil fuels.<sup>1</sup> Extensive effort has been devoted to developing technologies and devices to achieve economical hydrogen production, storage, and conversion.<sup>2</sup> Water electrolyzers and fuel cells have been identified as the most promising alternative energy conversion and storage devices based on highly efficient and clean electrochemical transformation reactions between hydrogen and water. The hydrogen evolution reaction (HER) occurs at the cathode of water electrolyzers using electricity from green energy inputs, whereas the hydrogen oxidation reaction (HOR) is an anodic process of fuel cells to convert hydrogen into electrical energy.<sup>3,4</sup> Recently, accompanied by the development of alkaline membranes, anion exchange membrane (AEM)-based electrolyzers and fuel cells have achieved appreciable progress in maximum current density and peak power density, which renders them promising alternatives to proton exchange membrane fuel cells (PEMFCs) with highly corrosive environments.<sup>5</sup> HOR and HER are crucial determinants of the energy efficiency of these devices because they operate in the reversible fuel cell, including fuel cell mode and electrolysis mode.<sup>3,6</sup> However, a sluggish alkaline HOR/HER on the anode of fuel cells turns into a “stumbling block”. As a result, there is an absolute need to develop highly robust HOR/HER electrocatalysts for alkaline media.

The alkaline HOR follows a two-step microscopic process, which involves the Tafel–Volmer or Heyrovsky–Volmer

sequences,<sup>7</sup> that is, H<sub>2</sub> dissociative adsorption form an intermediate (H<sub>ads</sub>) followed by oxidative desorption into a proton. The second step is that H<sub>ads</sub> either reacts with OH<sup>-</sup> in the solution or adsorbed OH (OH<sub>ads</sub>) to form H<sub>2</sub>O, from which two activity descriptors were proposed to explain sluggish alkali HOR kinetics: (1) HBE theory and (2) OH<sup>-</sup> adsorption (oxophilicity) theory.<sup>8–11</sup> Following the Sabatier principle, the optimal HOR/HER catalysts should be located near the vertex of the volcano plot with appropriate adsorbed HBE, such as Pt and Ir.<sup>12,13</sup> Yan<sup>8,14</sup> and Zhuang<sup>15</sup> et al. also showed that HBE is the major influencing factor on the HOR activity in alkaline environments. In contrast, Strmcnik et al. designed an advanced electrocatalyst using Pt–Ni (more oxophilic) alloy, concluding that the stronger OH<sup>-</sup> adsorption is favorable to HOR activity.<sup>16</sup> Furthermore, Markovic et al. deposited an OH<sup>-</sup> adsorption promoter Ni(OH)<sub>2</sub> on the Pt surface and reported a marked HOR activity enhancement compared with pristine Pt.<sup>17</sup> Accordingly, a mechanism of the delicate balance between HBE and OH<sup>-</sup> adsorption binding energy has been proposed for desirable HOR/HER electro-

Received: January 5, 2022

Accepted: February 24, 2022

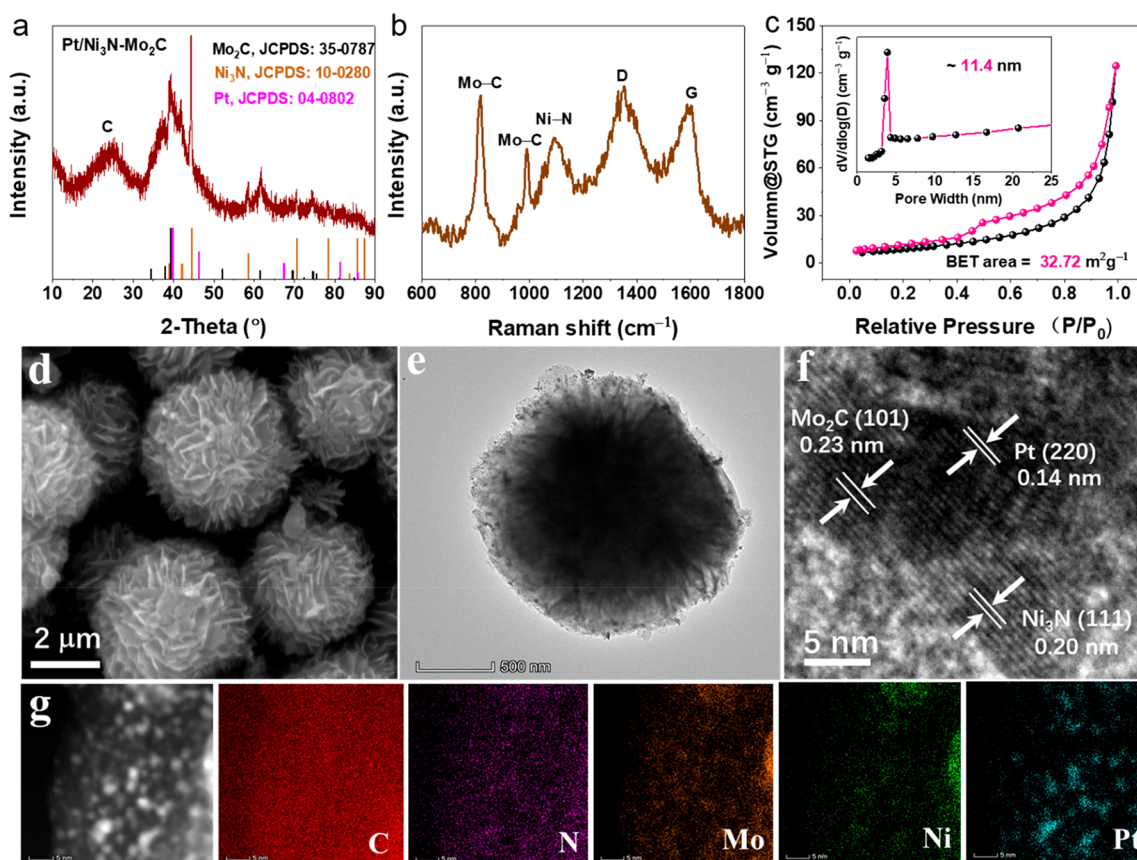


**Figure 1.** (a) XRD patterns; (b) Raman spectra; (c)  $N_2$  adsorption/desorption isotherms with the corresponding pore size distribution; (d) SEM, (e) TEM, (f) HR-TEM, and (g) HAADF-STEM images and elemental mappings of Pt/Ni<sub>3</sub>N–Mo<sub>2</sub>C.

catalysts in the base.<sup>16,18</sup> Nevertheless, a deep level of understanding of alkaline HOR/HER is still lacking.

Pt and Pt-based materials are used widely as the electrocatalysts for HOR/HER. Regrettably, commercial applications are limited by their scarcity and high cost.<sup>19</sup> To drive down the cost of HOR/HER electrocatalyst, one strategy is to create nonprecious metal active sites as an alternative to reduce Pt loading without compromising the activity.<sup>20</sup> Ni is abundant and more oxophilic than Pt, which could promote the OH adsorption significantly,<sup>13</sup> which renders Ni-based electrocatalysts promising components or catalyst supports in various precious-metal-containing catalysts for HOR/HER electrocatalysis.<sup>21,22</sup> Another strategy is to enhance the efficiency of noble metals. Numerous studies suggested that catalytic activities of noble metal particles strongly rely on their feature sizes.<sup>23</sup> During the catalytic processes, the reaction may generally occur at the catalyst surface interface instead of the whole particles; thus, reducing their dimension down to clusters to improve the metal utilization is particularly important.<sup>24</sup> However, the clusters' high surface free energy can hardly exist alone, which necessitates the development of efficient supports for stabilizing the small metal nanoparticles and inhibiting the nanoparticle aggregation through metal–support interactions.<sup>27</sup> Thus, the support-induced strategy comes to the fore. It is well-known that carbon black is an inexpensive, easily structured, and conductive material. Much previous work on alkaline HOR catalysis has focused on carbon-supported nanoparticles, but they have a weak catalyst–support interaction.<sup>25</sup> It has been reported that the metal nanoparticles tend to detach from the carbon support,

which is more serious in an alkaline electrolyte.<sup>26</sup> Early transition-metal carbides (TMCs; e.g., Mo<sub>2</sub>C and W<sub>2</sub>C) and nitrides (TMNs; e.g., Ni<sub>3</sub>N) have been extensively explored as standalone catalysts or supports in various noble-metal-containing catalysts owing to their high electrical conductivity, chemical stability, and earth abundance.<sup>27</sup> Furthermore, Liao et al. coated Pt layers on TMNs support, demonstrating an enhanced oxygen reduction reaction (ORR) by synergistic effects between Pt layers and the TMNs support.<sup>28</sup> Sanchez et al. investigated the impact of TMCs and TMNs supports on the thin Pt overlayers, in which the Pt electronic structure was modified by TMCs and TMNs, thereby tuning catalyst reactivity.<sup>29</sup> Therefore, Mo<sub>2</sub>C is used in this study to improve the catalyst conductivity and to create metal–support interaction that enhances the charge transfer between two species, which makes Mo<sub>2</sub>C a much better candidate than carbon materials.

Herein, we propose a facile method for synthesizing Pt nanoparticles anchored on Ni<sub>3</sub>N–Mo<sub>2</sub>C support (Pt/Ni<sub>3</sub>N–Mo<sub>2</sub>C) for HOR and HER catalysis in alkaline environments. In this Pt/Ni<sub>3</sub>N–Mo<sub>2</sub>C hybrid, the flower-like Ni<sub>3</sub>N–Mo<sub>2</sub>C microsphere was decorated with ~1.47 nm Pt nanoparticles. The achieved Pt/Ni<sub>3</sub>N–Mo<sub>2</sub>C demonstrated a good activity and high durability for HOR/HER, which showed a high HOR performance with a geometric exchange current density of 2.83 mA cm<sup>-2</sup> and a mass activity of 1.28 mA μg<sup>-1</sup>, which is superior to commercial Pt/C values. It also displayed encouraging HER with an overpotential as low as 11 mV at 10 mA cm<sup>-2</sup> and a small Tafel slope of 31.1 mV dec<sup>-1</sup>. DFT calculations and the detailed characterizations indicated that

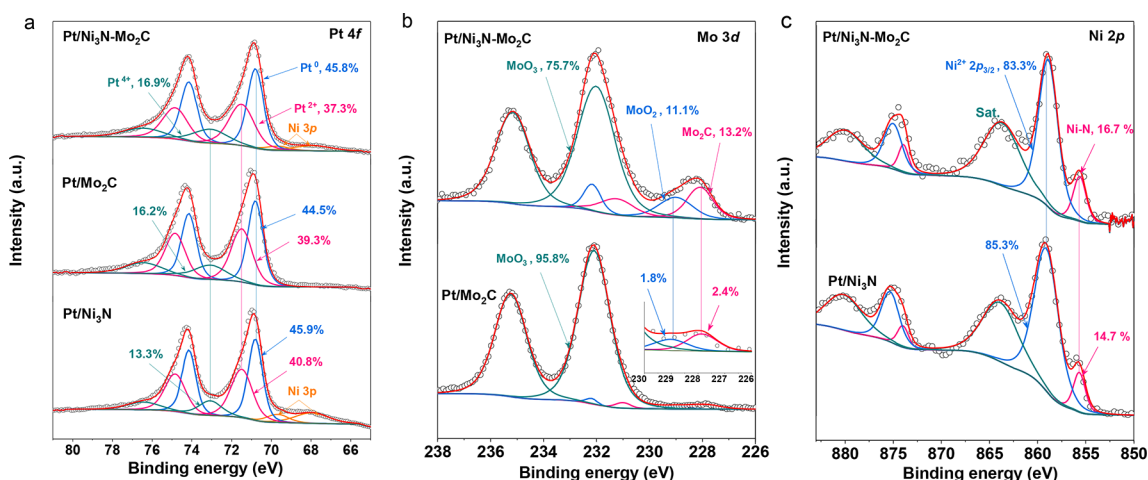


**Figure 2.** High-resolution XPS spectra of (a) Pt 4f + Ni 3p, (b) Mo 3d, and (c) Ni 2p regions in Pt/Ni<sub>3</sub>N–Mo<sub>2</sub>C, Pt/Mo<sub>2</sub>C, and Pt/Ni<sub>3</sub>N, respectively.

such outstanding HOR/HER performance was correlated with synergistic optimization of both suitable Pt–H<sub>ads</sub> and Ni<sub>3</sub>N–OH<sub>ads</sub> strengths, as well as Mo<sub>2</sub>C preferentially adsorbed and activated H<sub>2</sub>O molecules for dissociation and accessible active sites supplied by micro/nanostructure of Pt/Ni<sub>3</sub>N–Mo<sub>2</sub>C.

The Pt/Ni<sub>3</sub>N–Mo<sub>2</sub>C composite was prepared in three simple steps (see the Supporting Information for details). In the first step, (NH<sub>4</sub>)<sub>6</sub>Mo<sub>7</sub>O<sub>24</sub>·4H<sub>2</sub>O is used as the Mo source and dopamine hydrochloride (DA) as both the coordination ligand and N-containing carbon source.<sup>30</sup> Polymerization of DA with MoO<sub>4</sub><sup>2-</sup> was realized upon the addition of NH<sub>3</sub>·H<sub>2</sub>O initiator in a mixture of water and ethanol to derive Mo-polydopamine (Mo-PDA). The Mo-PDA was carburized at 850 °C for 3 h to convert into Mo<sub>2</sub>C. Thereafter, Ni(OH)<sub>2</sub> was fabricated by a hydrothermal process and blended with Mo<sub>2</sub>C in acetone under constant stirring, the Ni(OH)<sub>2</sub>–Mo<sub>2</sub>C composite was further annealed in an NH<sub>3</sub> atmosphere at 370 °C. Finally, the Pt nanoparticle-decorated Ni<sub>3</sub>N–Mo<sub>2</sub>C support was obtained following a simple wet-chemical route via mild H<sub>2</sub> reduction at room temperature.

The crystallographic texture of the substrate, precursor, and catalyst was elucidated by X-ray diffraction (XRD) patterns (Figures 1a and S2). The strong (002) graphite carbon diffraction peaks at approximately 26°,<sup>31</sup> where the diffraction peaks located at 34.3, 37.9, 39.4, 52.1, 61.5, 69.5, 74.6, and 75.5° correspond well to the (100), (002), (101), (102), (110), (103), (112), and (201) planes of hexagonal Mo<sub>2</sub>C (JCPDS No. 35-0787).<sup>32</sup> The characteristic peaks at 38.9, 42.1, 44.4, 58.5, 70.6, and 78.3° were assignable to the diffraction faces of (110), (002), (111), (112), (300), and (113) of hexagonal Ni<sub>3</sub>N (JCPDS No. 10-0280).<sup>33</sup> However, only a dominant peak in the diffraction pattern at 39.7° belonging to face-centered cubic (fcc) structured Pt was detected owing to the ultrafine and the ultralow Pt loading. Further insights regarding the structure and bonding environment were gained from Raman spectra. As showcased in Figure 1b, the two Raman bands at 823 and 1000 cm<sup>-1</sup> indicate the mode of Mo–C<sup>34</sup> and fingerprint bands characteristic of Ni–N at 1100 cm<sup>-1</sup>,<sup>35</sup> confirming the existence of Mo<sub>2</sub>C and Ni<sub>3</sub>N in hybrid Pt/Ni<sub>3</sub>N–Mo<sub>2</sub>C composite. Additionally, the D (1350 cm<sup>-1</sup>) to G (1580 cm<sup>-1</sup>) band intensity ratio of 1.02 indicated that the Pt reduction may have introduced some defects in the Ni<sub>3</sub>N–Mo<sub>2</sub>C. Subsequently, N<sub>2</sub> adsorption/desorption meas-

urements were conducted to evaluate the surface area and pore volume (Figure 1c). The Pt/Ni<sub>3</sub>N–Mo<sub>2</sub>C exhibited a type III curve,<sup>32</sup> and the corresponding BET surface area was 32.7 m<sup>2</sup> g<sup>-1</sup> with a pore size distribution of 11.4 nm. The mesopore structure is favorable for the exposure of active sites and consequently facilitates mass transport.<sup>36</sup>

The morphologies of the materials were characterized by scanning electron microscopy (SEM) and transmission electron microscopy (TEM). As depicted in Figure 1d, Pt/Ni<sub>3</sub>N–Mo<sub>2</sub>C presented a uniform flower-like morphology with a nanoflake surface and an average diameter of approximately 3 μm and displayed an intrinsic homogeneous feature of Mo<sub>2</sub>C microflowers on a large scale (Figure S3). The flower-like microspheres were constructed by numerous dense petals of a certain chrysanthemum to form a highly porous micro/nanostructure, allowing the reactants to access the active sites during the HOR/HER.<sup>37</sup> Observation via TEM (Figure 1e) revealed that a flower-like microspheres is uniformly decorated with Pt nanoparticles. As shown in Figure S4, the particle size of Pt on the Ni<sub>3</sub>N–Mo<sub>2</sub>C support is as small as 1.47 nm on average, whereas a larger average particle sizes of 2.09 and 3.03 nm were found on Ni<sub>3</sub>N and Mo<sub>2</sub>C single supports, respectively. The above results demonstrate that the size of Pt could be controlled by the Ni<sub>3</sub>N–Mo<sub>2</sub>C support, demonstrating significant synergism between Ni<sub>3</sub>N and Mo<sub>2</sub>C species. A high-resolution TEM (HR-TEM) image (Figure 1f) showed *d*-spacing of 0.23 nm corresponding to the (101) crystal face of hexagonal Mo<sub>2</sub>C,<sup>38</sup> and 0.20 nm was consistent with the (111) crystal plane of Ni<sub>3</sub>N.<sup>21</sup> The lattice fringes with a spacing of 0.144 nm were consistent with the Pt(220) plane.<sup>39</sup> Moreover, high-angle annular dark-field scanning transmission electron microscopy (HAADF-STEM) and corresponding energy-dispersive X-ray spectroscopy (EDX) mappings (Figure 1g) affirmed a uniform distribution of C, N, Mo, Ni, and Pt elements throughout the catalyst.

Additional characterization by X-ray photoelectron spectroscopy (XPS) was used to probe into the chemical composition and bonding states. The XPS survey scan of Pt/Ni<sub>3</sub>N–Mo<sub>2</sub>C unveiled that the surface was composed of C, N, Mo, Ni, and Pt elements (Figure S5). The core-level XPS C 1s spectra in Figure S6 deconvoluted into five peaks locating at 283.1, 284.0, 284.8, 286.0, and 288.2 eV, which were attributed to Mo–C, C=C, C–C, C–O, and C=O, respectively.<sup>32,40</sup>

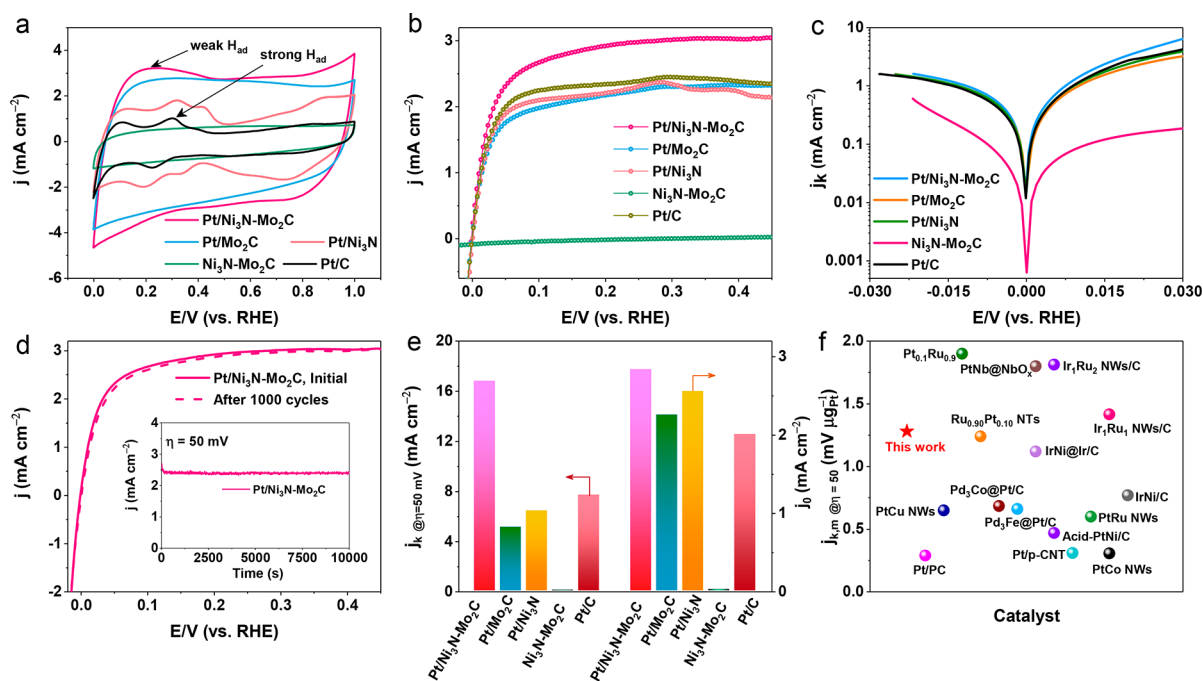


**Figure 3.** (a) CV curves in  $N_2$ -saturated 0.1 M KOH at a scan rate of  $50 \text{ mV s}^{-1}$ . (b) HOR polarization curves. (c) Representative HOR/HER Tafel plots of kinetic current density ( $j_k$ ) of studied catalysts. (d) Accelerated durability test results and chronoamperometric responses of Pt/ $Ni_3N$ - $Mo_2C$ . (e) Comparison of the  $j_k$  at 50 mV and the exchange current density ( $j_0$ ) of different catalysts. (f) Comparison of mass activity at 50 mV ( $j_{k,m}@50 \text{ mV}$ ) with previous reports.

Similarly, the high-resolution Pt 4f + Ni 3p spectrum of Pt/ $Ni_3N$ - $Mo_2C$  was deconvoluted in Figure 2a. The two crucial peaks at 70.8 and 74.6 eV binding energies coincide with metallic  $Pt^0$ , whereas the peaks located at 71.5 and 74.9 eV can be attributed to  $Pt^{2+}$ ; the peaks at 73.0 and 76.5 eV correspond to  $Pt^{4+}$  species. The XPS results showed clear dominance of metallic  $Pt^0$  at 45.8 and 45.9 atomic percentage (%) on the surface of Pt/ $Ni_3N$ - $Mo_2C$  and Pt/ $Ni_3N$ , which are higher than that of Pt/ $Mo_2C$  (44.5%) catalyst, revealing the  $Ni_3N$  surface contributes to the redox reaction between  $H_2$  and Pt(IV) in solution.<sup>41</sup> This also implied that reciprocal electronic interaction between Pt nanoparticles and support was a major contributor to the variation percentages. In the Ni 2p region, the two peaks at 67.8 and 69.3 eV can be indexed to Ni 3p<sub>3/2</sub> and Ni 3p<sub>1/2</sub>, indicating the strong interaction between Pt nanoparticles and the  $Ni_3N$  phase.<sup>42</sup> As shown in Figure 2b, the deconvoluted high-resolution Mo 3d spectrum divided the contribution from  $Mo_2C$  ( $d_{5/2}$  at 228.1 eV),  $MoO_2$  ( $d_{5/2}$  at 229.1 eV), and  $MoO_3$  ( $d_{5/2}$  at 232.0 eV). The results indicated that the  $Mo_2C$  content in Pt/ $Ni_3N$ - $Mo_2C$  is 13.2%, which is significantly higher than that in Pt/ $Mo_2C$  (2.4%); the high electrical conductivity of  $Mo_2C$  enhanced electron transfer and reduced interfacial impedance.<sup>27</sup> The presence of oxide is generally unavoidable because of the pyrophoricity in areal exposure to air.<sup>43</sup> It must be remarked that we can see clear  $Mo_2C$  characteristic peaks in the XRD spectrum, which further proves that only the sample surface is oxidized. Samples were characterized with XPS to identify the oxygen-containing surface species. Figure 2c shows the Ni 2p high-resolution spectrum; the peaks located at 852.9, 856.5, and 862.2 eV can be ascribed to Ni-N,  $Ni^{2+}$ , and the satellite peak.<sup>44</sup> The peaks at 856.5 eV can be assigned to  $Ni^{2+}$ , which are possibly derived from the surface oxidation and the compact oxide layer formed at the surface of catalyst that is

thicker than the penetration depth of XPS (about 10 nm). This oxide layer arises because O elements come from various sources.  $Mo_2C$  and  $Ni_3N$  experience areal exposure to air, resulting in gradual surface oxidation. Thus, the presence of a significant amount of superficial oxides is not surprising and practically inescapable. The area percentage of Ni-N species in Pt/ $Ni_3N$ - $Mo_2C$  (16.7%) is higher than that of Pt/ $Ni_3N$  (14.7%), indicating higher catalytic performance. XPS peaks of N 1s were detected at 394.3, 397.9, and 400.1 eV, signifying Mo 3p, N-metal bonding/pyridinic-N, and N-H bonding/pyrrolic-N (Figure S7).<sup>45</sup>

The HOR was evaluated in  $H_2$ -saturated 0.1 M KOH by casting a thin catalyst layer onto a rotating disk electrode (RDE). Noticeably, the reversible hydrogen electrode (RHE) was calibrated (Figure S1), and all potentials were measured against RHE. In addition, the electrochemical data are presented with  $iR$  correction (Figure S10). The optimized Pt doping content and the corresponding performance parameters are shown in Figure S8. The results showed that the best catalyst, designated as Pt/ $Ni_3N$ - $Mo_2C$ , had the Pt content of 6.39 wt %. Pt/ $Ni_3N$ - $Mo_2C$  is the target catalyst discussed below if not explicitly stated.

Cyclic voltammetry (CVs) curves were recorded in  $N_2$ -saturated 0.1 M KOH solution to study hydrogen adsorption/desorption behaviors to understand the alkaline HOR mechanism. The CVs between 0 and 0.45 V vs RHE corresponded to the hydrogen region, which was in agreement with the hydrogen under-potential deposition ( $H_{upd}$ ) region of Pt.<sup>8,46</sup> In previous studies, the  $H_{upd}$  peak's potential has a direct correlation with HBE.<sup>46,47</sup> As illustrated in Figure 3a, a negative shift was found for the  $H_{upd}$  peak's potential from Pt/ $Ni_3N$  (0.312 V), Pt/ $Mo_2C$  (0.247 V), to Pt/ $Ni_3N$ - $Mo_2C$  (0.218 V), suggesting Pt/ $Ni_3N$ - $Mo_2C$  has weaker hydrogen-bonding sites that lead to faster HOR

Table 1. Summary of ECSA,  $j_{k,m}$ , SA,  $j_k$ , and  $j_0$  of Different Catalysts in This Work<sup>a</sup>

catalyst	ECSA (m <sup>2</sup> g <sup>-1</sup> )	$j_{k,m}$ (mA μg <sup>-1</sup> )	SA (mA cm <sup>-2</sup> )	$j_k$ (mA cm <sup>-2</sup> )	$j_0$ (mA cm <sup>-2</sup> )
Pt/C	80.2	0.25	0.31	7.65	1.9
Pt/Ni <sub>3</sub> N–Mo <sub>2</sub> C	101.2	1.28	0.51	16.75	2.83
Pt/Mo <sub>2</sub> C	47.6	0.36	0.33	5.09	2.25
Pt/Ni <sub>3</sub> N	60.3	0.35	0.32	6.39	2.55
Pt <sub>1.5</sub> /Ni <sub>3</sub> N–Mo <sub>2</sub> C	50.9	0.39	0.14	1.2	0.83
Pt <sub>3.7</sub> /Ni <sub>3</sub> N–Mo <sub>2</sub> C	64.7	0.27	0.19	2.03	0.94
Pt <sub>8.3</sub> /Ni <sub>3</sub> N–Mo <sub>2</sub> C	87.4	0.53	0.31	8.97	2.49

<sup>a</sup> $j_{k,m}$ : mass activity at 50 mV. SA: specific activity.  $j_k$ : kinetic current density at 50 mV.  $j_0$ : exchange current density from the micropolarization region (−5 to 5 mV) by linear fitting through the Butler–Volmer equation.

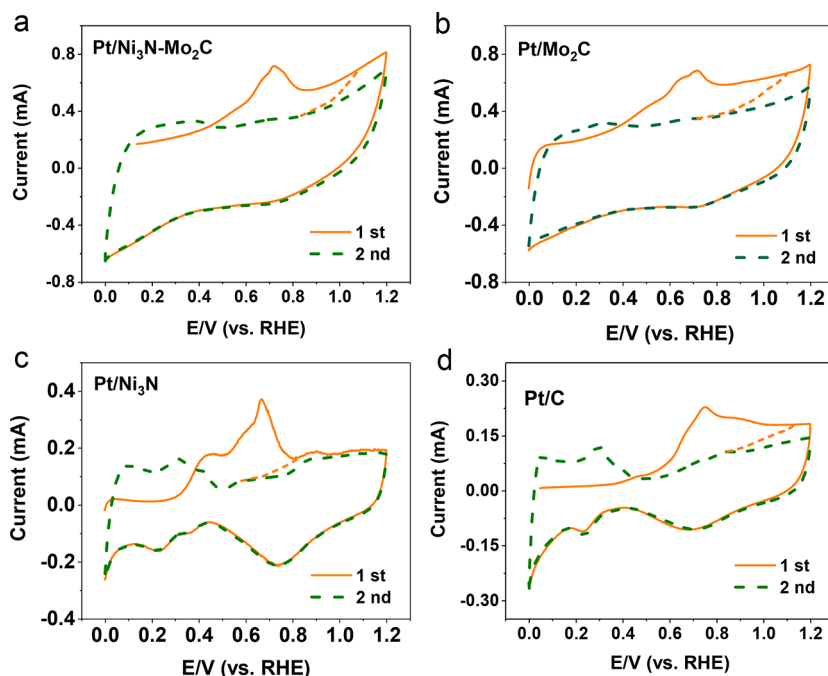
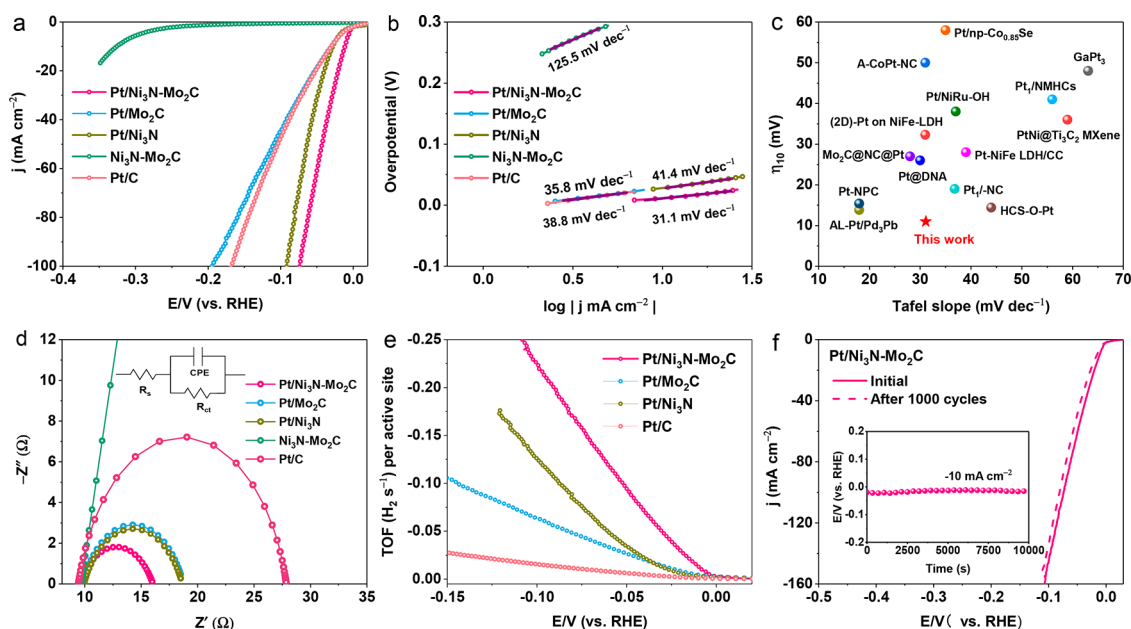


Figure 4. CO-stripping voltammetry of (a) Pt/Ni<sub>3</sub>N–Mo<sub>2</sub>C, (b) Pt/Mo<sub>2</sub>C, (c) Pt/Ni<sub>3</sub>N, and (d) Pt/C in 0.1 M KOH.

kinetics.<sup>48</sup> However, Ni<sub>3</sub>N–Mo<sub>2</sub>C showed unobvious hydrogen adsorption/desorption processes, indicating that Pt is the predominant activity center and served as an active site for the hydrogen intermediate.<sup>10,11</sup> Besides, the highest CV charge of Pt/Ni<sub>3</sub>N–Mo<sub>2</sub>C is attributed to the better Pt dispersion and stability on Ni<sub>3</sub>N–Mo<sub>2</sub>C supports. Simultaneously, it also illustrated the strong synergistic interaction between Ni<sub>3</sub>N and Mo<sub>2</sub>C species. The HOR polarization curves were tested in H<sub>2</sub>-saturated 0.1 M KOH solution at the rotation speed of 1600 rpm. Figure 3b shows that Pt/Ni<sub>3</sub>N–Mo<sub>2</sub>C possessed the onset potential of HOR as low as 0 V vs RHE, highlighting its significant energetics for alkaline HOR.<sup>25,49</sup> Furthermore, Pt/Ni<sub>3</sub>N–Mo<sub>2</sub>C achieved the highest current density of anodic hydrogen oxidation at the whole potential range, which evidenced the extraordinary HOR activity of Pt/Ni<sub>3</sub>N–Mo<sub>2</sub>C. By contrast, Ni<sub>3</sub>N–Mo<sub>2</sub>C was shown to be nearly inactive toward HOR, substantiating the remarkable synergistic effects and electronic interaction of Pt nanoparticles and Ni<sub>3</sub>N–Mo<sub>2</sub>C support to tune catalyst reactivity in promoting hydrogen oxidation.<sup>29,50</sup> To further confirm whether the H<sub>2</sub> can be used as a reductant to reduce Pt(IV) in the precursor solution at ambient temperature, ICP-AES was performed. We detected only a small amount of Pt with 0.42 wt % (Table S1) without an H<sub>2</sub> environment, and the catalyst presented a minimal HOR activity. Instead, 6.39 wt % Pt was deposited on

Pt/Ni<sub>3</sub>N–Mo<sub>2</sub>C under H<sub>2</sub> atmosphere, and it showed much higher HOR activity (Figure S11). The Pt loadings of Pt/Ni<sub>3</sub>N–Mo<sub>2</sub>C, Pt/Mo<sub>2</sub>C, and Pt/Ni<sub>3</sub>N were measured as 6.39, 6.95, and 9.04 wt % by ICP. Although the Pt/Ni<sub>3</sub>N has the highest Pt loading, the Pt-decorated Ni<sub>3</sub>N–Mo<sub>2</sub>C support shows the best HOR/HER performance. Moreover, the average Pt particle size of Pt/Ni<sub>3</sub>N–Mo<sub>2</sub>C is much smaller than those of Pt/Mo<sub>2</sub>C and Pt/Ni<sub>3</sub>N (Figure S4), showing the significant effect of the support and suggesting a unique synergistic effect between Pt, Ni<sub>3</sub>N, and Mo<sub>2</sub>C. Figure S12 shows that the Pt/Ni<sub>3</sub>N–Mo<sub>2</sub>C had a negligible effect on current density in N<sub>2</sub>-saturated 0.1 M KOH at 1600 rpm, thus corroborating the catalytic reaction of HOR.<sup>47</sup> Next, we investigated the polarization curves of the target catalyst at different rotating speeds, where the plateau current density grows with increasing rotation speed owing to improved mass transport (Figure S13).<sup>51</sup> We also show the mass transport-corrected kinetic current density of these catalysts (Figure 3c). Tafel plots validated the fastest HOR kinetics on Pt/Ni<sub>3</sub>N–Mo<sub>2</sub>C. The long-term durability of Pt/Ni<sub>3</sub>N–Mo<sub>2</sub>C and the associated ability to continuously catalyze H<sub>2</sub> oxidation were assessed employing chronoamperometry ( $j \sim t$ ) at  $\eta = 50$  mV and polarization curves after 1000 CV scans. As presented in Figure 3d, the two polarization curves almost overlap, and the Pt/Ni<sub>3</sub>N–Mo<sub>2</sub>C delivered a stable current density without



**Figure 5.** (a) HER performance in  $\text{H}_2$ -saturated 0.1 M KOH and (b) corresponding Tafel plots with associated linear fittings. (c) Comparison of overpotential@ $10 \text{ mA cm}^{-2}$  with previous reports. (d) Complex-plane plots of electrochemical impedance spectra and (e) TOF per surface metal site of different electrocatalysts. (f) Durability test for Pt/ $\text{Ni}_3\text{N-Mo}_2\text{C}$ .

noticeable decay. The Pt/ $\text{Ni}_3\text{N-Mo}_2\text{C}$  exhibited the highest  $j_k$  ( $16.75 \text{ mA cm}^{-2}$ ) at 50 mV in contrast to those of Pt/ $\text{Mo}_2\text{C}$  ( $5.09 \text{ mA cm}^{-2}$ ), Pt/ $\text{Ni}_3\text{N}$  ( $6.39 \text{ mA cm}^{-2}$ ), and Pt/C ( $7.65 \text{ mA cm}^{-2}$ ). Meanwhile, a geometric  $j_0$  of Pt/ $\text{Ni}_3\text{N-Mo}_2\text{C}$  reached  $2.83 \text{ mA cm}^{-2}$ , outperforming those of Pt/ $\text{Mo}_2\text{C}$  ( $2.25 \text{ mA cm}^{-2}$ ), Pt/ $\text{Ni}_3\text{N}$  ( $2.55 \text{ mA cm}^{-2}$ ), and Pt/C ( $1.9 \text{ mA cm}^{-2}$ ) (Figures 3e and S9). As shown in Figure 3f and Table S2, Pt/ $\text{Ni}_3\text{N-Mo}_2\text{C}$  showed higher mass activity at 50 mV, substantially exceeding reported well-known catalysts. Moreover, the HOR performance parameters of all catalysts are given in Table 1. CO stripping voltammetry was used to calculate the ECSA value. The ECSA of Pt/ $\text{Ni}_3\text{N-Mo}_2\text{C}$  was calculated to be  $101.2 \text{ m}^2 \text{ g}^{-1}$ , which represented 2.1-, 1.7-, and 1.3-fold increase compared with those of Pt/ $\text{Mo}_2\text{C}$  ( $47.6 \text{ m}^2 \text{ g}^{-1}$ ), Pt/ $\text{Ni}_3\text{N}$  ( $60.3 \text{ m}^2 \text{ g}^{-1}$ ), and Pt/C ( $80.2 \text{ m}^2 \text{ g}^{-1}$ ) (Figures 4 and S14).

The HER activities of as-made electrocatalysts were evaluated by linear sweep voltammetry (LSV) in  $\text{H}_2$ -saturated 0.1 M KOH with a scan rate of  $10 \text{ mV s}^{-1}$  at 1600 rpm. The Pt loading was optimized, and concise performance parameters are shown in Figure S15. The Pt/ $\text{Ni}_3\text{N-Mo}_2\text{C}$  exhibited an ultralow overpotential of 11 mV @  $10 \text{ mA cm}^{-2}$  and the smallest Tafel slope as well. We next examined the HER activities of Pt/ $\text{Ni}_3\text{N-Mo}_2\text{C}$  in greater detail, being associated with Pt/ $\text{Mo}_2\text{C}$ , Pt/ $\text{Ni}_3\text{N}$ , and Pt/C as references. As shown in Figure 5a, Pt/ $\text{Ni}_3\text{N-Mo}_2\text{C}$  presented substantially better electrocatalytic activities in comparison to that of contrastive samples; only 11 mV was needed to achieve  $10 \text{ mA cm}^{-2}$ , which was lower than for Pt/ $\text{Mo}_2\text{C}$  (32 mV), Pt/ $\text{Ni}_3\text{N}$  (28 mV), and Pt/C (31 mV). The  $\text{Ni}_3\text{N-Mo}_2\text{C}$  was inert for HER catalysis. To assess the underlying reaction kinetics, Tafel plots are presented in Figure 5b. The Tafel slopes decreased in the order 125.5, 41.4, 38.8, 35.8, and 31.1  $\text{mV dec}^{-1}$  for  $\text{Ni}_3\text{N-Mo}_2\text{C}$ , Pt/ $\text{Ni}_3\text{N}$ , Pt/C, Pt/ $\text{Mo}_2\text{C}$ , and Pt/ $\text{Ni}_3\text{N-Mo}_2\text{C}$ , which demonstrated the facilitation of the hydrogen evolution kinetics. Notably, Pt/ $\text{Ni}_3\text{N-Mo}_2\text{C}$  underwent the Volmer-Tafel mechanism where the recombination of absorbed H is

the rate-determining step.<sup>52</sup> Compared to other recently reported catalysts (Figure 5c and Table S3), the Pt/ $\text{Ni}_3\text{N-Mo}_2\text{C}$  possessed outstanding HER activity. As illustrated in Figure 5d, the Pt/ $\text{Ni}_3\text{N-Mo}_2\text{C}$  showed the smallest semicircle in the Nyquist spectra, implying good charge transferability.<sup>53</sup> To quantitatively probe the information about the intrinsic activity, the turnover frequencies were calculated using ICP results.<sup>54</sup> As seen in Figure 5e, the TOF value of Pt/ $\text{Ni}_3\text{N-Mo}_2\text{C}$  was  $0.23 \text{ H}_2 \text{ s}^{-1}$  at 100 mV vs RHE, which was higher than that of Pt/ $\text{Ni}_3\text{N}$  ( $0.13 \text{ H}_2 \text{ s}^{-1}$ ), Pt/ $\text{Mo}_2\text{C}$  ( $0.07 \text{ H}_2 \text{ s}^{-1}$ ), and Pt/C ( $0.03 \text{ H}_2 \text{ s}^{-1}$ ), clearly indicating  $\text{Ni}_3\text{N-Mo}_2\text{C}$  could serve a supporting scaffold for Pt nanoparticles to intrinsically improve the HER activity. The long-term stability was evaluated (Figure 5f), and the HER performance of Pt/ $\text{Ni}_3\text{N-Mo}_2\text{C}$  was well maintained after 1000 CV scans with a negligible change in the LSV curves. In addition, Pt/ $\text{Ni}_3\text{N-Mo}_2\text{C}$  delivered a stable potential at  $-10 \text{ mA cm}^{-2}$  throughout the test, verifying excellent stability.

The Pt/ $\text{Ni}_3\text{N-Mo}_2\text{C}$  hybrid is a three-component catalyst in which each component plays a separate role. The Pt/ $\text{Ni}_3\text{N-Mo}_2\text{C}$  showed notable HOR/HER performance that can be correlated with the combined effects of the following features.

(1) We noted that both  $\text{H}_{\text{ads}}$  and  $\text{OH}_{\text{ads}}$  are the activity descriptors for HOR catalysis.<sup>10,55</sup> In the UPD-H region of the CV curve (Figure 3a), the peak at low potential corresponds to H adsorption/desorption at the Pt metal sites (weakly bonded H). Considering that CO can adsorb specifically onto many metal surfaces,<sup>8</sup> we thus employed CO-stripping experiments to characterize the OH adsorption on the catalyst's surface because  $\text{OH}_{\text{ads}}$  facilitates removing the  $\text{CO}_{\text{ad}}$  intermediate on the Pt surface.<sup>49</sup> Figure 4 reveals that the CO stripping peak potential of Pt/ $\text{Ni}_3\text{N-Mo}_2\text{C}$  located at 0.71 V and Pt/ $\text{Mo}_2\text{C}$  displayed a peak at 0.72 V. Compared with the two catalysts, Pt/ $\text{Ni}_3\text{N}$  showed a lower CO oxidation peak at 0.66 V, indicating the stronger OH adsorption sites supplied by oxophilic  $\text{Ni}_3\text{N}$  moieties.<sup>56</sup> To gain a clearer view regarding the possible active sites of Pt/ $\text{Ni}_3\text{N-Mo}_2\text{C}$  and the mechanism

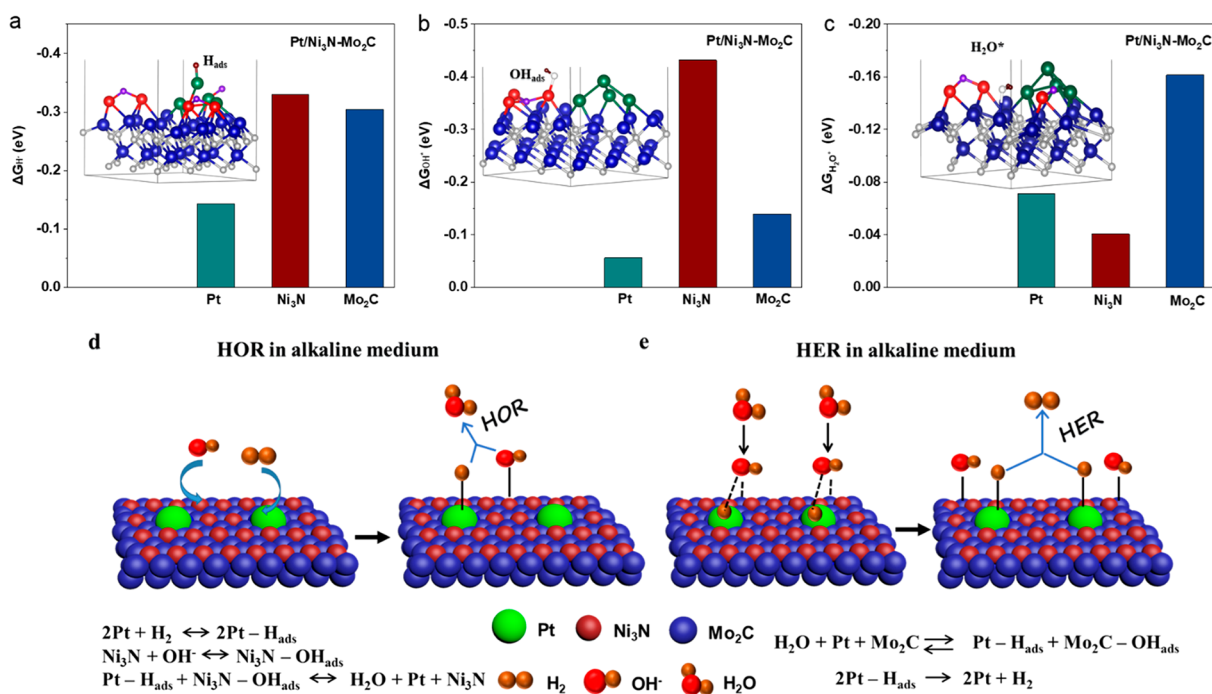


**Figure 6.** Theoretical calculation results. (a) Gibbs free energy profiles for hydrogen adsorption ( $\Delta G_{H^*}$ ). The inset illustrates optimized hydrogen adsorption configuration on Pt sites. (b) Gibbs free energy profiles for hydroxyl adsorption ( $\Delta G_{OH^*}$ ). The inset illustrates optimized hydroxyl adsorption configuration on Ni<sub>3</sub>N sites. (c) Water adsorption energy on Pt, Ni<sub>3</sub>N, and Mo<sub>2</sub>C in Pt/Ni<sub>3</sub>N-Mo<sub>2</sub>C. The inset illustrates optimized water adsorption configuration on Mo<sub>2</sub>C sites. Schematic diagram for (d) HOR and (e) HER mechanism in alkaline medium at Pt/Ni<sub>3</sub>N-Mo<sub>2</sub>C electrode.

underlying the notable HOR/HER activity, DFT calculations were performed. We initially constructed and optimized catalytic models of Pt/Ni<sub>3</sub>N-Mo<sub>2</sub>C to represent the catalytic surface, as presented in Figures S16–S19. Pt/Ni<sub>3</sub>N-Mo<sub>2</sub>C possessed optimal adsorption sites of H<sub>ads</sub> and OH<sub>ads</sub>. As shown in Figure 6a, Pt in Pt/Ni<sub>3</sub>N-Mo<sub>2</sub>C shows an ideal hydrogen intermediate adsorption energy ( $\Delta G_{H^*}$ ) of  $-0.14$  eV, which was closer to the theoretical optimal value ( $\Delta G_{H^*} = 0$  eV) for both HOR and HER compared to Ni<sub>3</sub>N ( $-0.32$  eV) or Mo<sub>2</sub>C ( $-0.30$  eV) in Pt/Ni<sub>3</sub>N-Mo<sub>2</sub>C. This result indicates the H\* adsorption takes place on the Pt site,<sup>57</sup> matching the experimental data quite well. Further, the adsorption free energies of OH\* ( $\Delta G_{OH^*}$ ) on Pt/Ni<sub>3</sub>N-Mo<sub>2</sub>C were also calculated (Figure 6b).  $\Delta G_{OH^*}$  was calculated to be  $-0.43$  eV on Ni<sub>3</sub>N in Pt/Ni<sub>3</sub>N-Mo<sub>2</sub>C, which displayed more assertive adsorption behavior than that of Pt ( $-0.06$  eV) and Mo<sub>2</sub>C ( $-0.14$  eV), suggesting that surface OH\* binds to the highly oxophilic Ni<sub>3</sub>N. Thus, the Pt–Ni<sub>3</sub>N interface offers dissociative-adsorption of H<sub>2</sub> to form H<sub>ads</sub> intermediate (Pt–H<sub>ads</sub>) and provides OH adsorption sites to form Ni<sub>3</sub>N–OH<sub>ads</sub>. Next, the H<sub>ads</sub> reacts with the adjacent OH<sub>ads</sub> to form H<sub>2</sub>O.<sup>58</sup> For the HER mechanism, as the most important step of HER, Mo<sub>2</sub>C in Pt/Ni<sub>3</sub>N-Mo<sub>2</sub>C exhibits the strongest energy barriers of H<sub>2</sub>O adsorption compared to Pt and Ni<sub>3</sub>N (Figure 6c), which facilitated the breaking of HO–H bonds in H<sub>2</sub>O,<sup>59</sup> to form adsorbed H atoms on neighboring Pt sites and recombine to form H<sub>2</sub>.<sup>10</sup> Thus, a bifunctional mechanism is proposed for enhanced HOR/HER activity of Pt/Ni<sub>3</sub>N-Mo<sub>2</sub>C in an alkaline medium, as shown in Figure 6d,e.

(2) XPS study was performed to gain insights into the metal–support interactions in different Pt samples. The XPS results indicated a strong Pt/Ni<sub>3</sub>N-Mo<sub>2</sub>C electronic interaction between Pt and Ni<sub>3</sub>N-Mo<sub>2</sub>C.

(3) Systematic electrochemical experiments reveal that Pt/Ni<sub>3</sub>N-Mo<sub>2</sub>C showed the best HOR/HER performance. At the same time, Ni<sub>3</sub>N-Mo<sub>2</sub>C were shown to be nearly inactive toward HOR/HER, and Pt/Ni<sub>3</sub>N-Mo<sub>2</sub>C has better performance than Pt/C, indicating not only that the Pt is the active site but also that there is a synergy between the Pt and Ni<sub>3</sub>N-Mo<sub>2</sub>C support.

(4) Furthermore, Pt/Ni<sub>3</sub>N-Mo<sub>2</sub>C achieved the highest current density of HOR/HER compared with Pt/Mo<sub>2</sub>C and Pt/Ni<sub>3</sub>N, once again confirming the synergistic effects between Ni<sub>3</sub>N and Mo<sub>2</sub>C species.

(5) The highest CV charge follows the sequence of Pt/Ni<sub>3</sub>N-Mo<sub>2</sub>C > Pt/Mo<sub>2</sub>C > Pt/Ni<sub>3</sub>N, revealing the Mo<sub>2</sub>C provided high electrical conductivity and the solid synergistic interaction between Ni<sub>3</sub>N and Mo<sub>2</sub>C species.

(6) The highly porous micro/nanostructure of Pt/Ni<sub>3</sub>N-Mo<sub>2</sub>C engenders more exposed active sites and favors the close contact with electrolytes to enable more efficient transport of electrons.

We developed a simple and effective approach to fabricate Pt nanoparticle-decorated micro/nanostructured Ni<sub>3</sub>N-Mo<sub>2</sub>C microsphere with a fascinating order and hierarchy over nanoscale, mesoscale, and microscale. The submicrometer Ni<sub>3</sub>N-Mo<sub>2</sub>C support favors the Pt nanoparticle adsorption, creating an interaction mechanism and ultimately decreasing Pt loading. The ideal Ni<sub>3</sub>N-Mo<sub>2</sub>C support controls the size of Pt within 2 nm and suppresses the extensive agglomeration of Pt nanoparticles during the H<sub>2</sub> reduction, promotes OH adsorption/H<sub>2</sub>O dissociation sites, and provides high electrical conductivity for Pt/Ni<sub>3</sub>N-Mo<sub>2</sub>C. The optimized Pt/Ni<sub>3</sub>N-Mo<sub>2</sub>C exhibited impressive performance toward alkaline HOR/HER by showing a higher mass activity and exchange current density of HOR, excellent HER with ultralow

overpotential at 10 mA cm<sup>-2</sup>, and higher TOF value compared to the commercial Pt/C. Characteristic studies certified that the strong interaction between Pt nanoparticles and the support enabled more active sites and reaction centers. Therefore, it activated H<sub>2</sub> dissociation to form Pt–H<sub>ads</sub>, which reacts with Ni<sub>3</sub>N–OH<sub>ads</sub> to form H<sub>2</sub>O, and Mo<sub>2</sub>C can theoretically serve as the promoted H<sub>2</sub>O adsorption and dissociation site, as demonstrated by DFT calculations, leading to the outstanding HOR and HER activities. This work may open up opportunities for developing bifunctional alkaline HOR/HER catalysts.

## ■ ASSOCIATED CONTENT

### SI Supporting Information

The Supporting Information is available free of charge at <https://pubs.acs.org/doi/10.1021/acs.jpcllett.2c00021>.

Details on materials, synthesis procedures, characterization, electrochemical measurements, impedance spectroscopy study, and HOR and HER comparison tables (PDF)

## ■ AUTHOR INFORMATION

### Corresponding Authors

**Tayirjan Taylor Isimjan** – Saudi Arabia Basic Industries Corporation (SABIC) at King Abdullah University of Science and Technology (KAUST), Thuwal 23955-6900, Saudi Arabia; [orcid.org/0000-0003-1735-481X](https://orcid.org/0000-0003-1735-481X); Email: [isimjant@sabic.com](mailto:isimjant@sabic.com)

**Xiulin Yang** – Guangxi Key Laboratory of Low Carbon Energy Materials, School of Chemistry and Pharmaceutical Sciences, Guangxi Normal University, Guilin 541004, People's Republic of China; [orcid.org/0000-0003-2642-4963](https://orcid.org/0000-0003-2642-4963); Email: [xlyang@gxnu.edu.cn](mailto:xlyang@gxnu.edu.cn)

### Authors

**Yuting Yang** – Guangxi Key Laboratory of Low Carbon Energy Materials, School of Chemistry and Pharmaceutical Sciences, Guangxi Normal University, Guilin 541004, People's Republic of China

**Qiumei Dai** – Guangxi Key Laboratory of Low Carbon Energy Materials, School of Chemistry and Pharmaceutical Sciences, Guangxi Normal University, Guilin 541004, People's Republic of China

**Luyan Shi** – Guangxi Key Laboratory of Low Carbon Energy Materials, School of Chemistry and Pharmaceutical Sciences, Guangxi Normal University, Guilin 541004, People's Republic of China

**Yi Liu** – Guangxi Key Laboratory of Low Carbon Energy Materials, School of Chemistry and Pharmaceutical Sciences, Guangxi Normal University, Guilin 541004, People's Republic of China

Complete contact information is available at: <https://pubs.acs.org/doi/10.1021/acs.jpcllett.2c00021>

### Notes

The authors declare no competing financial interest.

## ■ ACKNOWLEDGMENTS

This work has been supported by the National Natural Science Foundation of China (No. 21965005), Natural Science Foundation of Guangxi Province (2018GXNSFAA294077 and 2021GXNSFAA076001), Project of High-Level Talents

of Guangxi (F-KA18015), and Guangxi Technology Base and Talent Subject (GUIKEAD18126001 and GUIKEAD20297039).

## ■ REFERENCES

- (1) Xiong, B.; Jin, B.; Zhao, W.; Zhou, H.; Luo, J.; Si, D.; Chen, L.; Shi, J. NiMo Nanoparticles Anchored on N-Doped Carbon Rods for High-Efficiency Hydrogen Electrooxidation in Alkaline Media. *ACS Appl. Mater. Interfaces* **2021**, *13*, 15475–15481.
- (2) Strmcnik, D.; Escudero-Escribano, M.; Kodama, K.; Stamenkovic, V. R.; Cuesta, A.; Marković, N. M. Enhanced Electrocatalysis of the Oxygen Reduction Reaction Based on Patterning of Platinum Surfaces with Cyanide. *Nat. Chem.* **2010**, *2*, 880–885.
- (3) Huang, G.; Liang, W.; Wu, Y.; Li, J.; Jin, Y. Q.; Zeng, H.; Zhang, H.; Xie, F.; Chen, J.; Wang, N.; et al. Co<sub>2</sub>P/CoP Hybrid as a Reversible Electrocatalyst for Hydrogen Oxidation/Evolution Reactions in Alkaline Medium. *J. Catal.* **2020**, *390*, 23–29.
- (4) Tian, X.; Zhao, P.; Sheng, W. Hydrogen Evolution and Oxidation: Mechanistic Studies and Material Advances. *Adv. Mater.* **2019**, *31*, 1808066.
- (5) Chung, H. T.; Martinez, U.; Matanovic, I.; Kim, Y. S. Cation–Hydroxide–Water Coadsorption Inhibits the Alkaline Hydrogen Oxidation Reaction. *J. Phys. Chem. Lett.* **2016**, *7*, 4464–4469.
- (6) Chen, G.; Delafuente, D. A.; Sarangapani, S.; Mallouk, T. E. Combinatorial Discovery of Bifunctional Oxygen Reduction — Water Oxidation Electrocatalysts for Regenerative Fuel Cells. *Catal. Today* **2001**, *67*, 341–355.
- (7) Xiong, B.; Zhao, W.; Chen, L.; Shi, J. One-Step Synthesis of W<sub>2</sub>C@N,P-C Nanocatalysts for Efficient Hydrogen Electrooxidation across the Whole pH Range. *Adv. Funct. Mater.* **2019**, *29*, 1902505.
- (8) Zheng, J.; Sheng, W.; Zhuang, Z.; Xu, B.; Yan, Y. Universal Dependence of Hydrogen Oxidation and Evolution Reaction Activity of Platinum-Group Metals on pH and Hydrogen Binding Energy. *Sci. Adv.* **2016**, *2*, e1501602.
- (9) Sheng, W.; Zhuang, Z.; Gao, M.; Zheng, J.; Chen, J. G.; Yan, Y. Correlating Hydrogen Oxidation and Evolution activity on Platinum at Different pH with Measured Hydrogen Binding Energy. *Nat. Commun.* **2015**, *6*, 5848.
- (10) Kundu, M. K.; Bhowmik, T.; Mishra, R.; Barman, S. Platinum Nanostructure/Nitrogen-Doped Carbon Hybrid: Enhancing its Base Media HER/HOR Activity through Bi-functionality of the Catalyst. *ChemSusChem* **2018**, *11*, 2388–2401.
- (11) Samanta, R.; Mishra, R.; Barman, S. Interface- and Surface-Engineered PdO–RuO<sub>2</sub> Hetero-Nanostructures with High Activity for Hydrogen Evolution/Oxidation Reactions. *ChemSusChem* **2021**, *14*, 2112–2125.
- (12) Norskov, J. K.; Bligaard, T.; Logadottir, A.; Kitchin, J. R.; Chen, J. G.; Pandalov, S.; Stimming, U. Trends in the Exchange Current for Hydrogen Evolution. *J. Electrochem. Soc.* **2005**, *152*, J23.
- (13) Lu, S.; Zhuang, Z. Investigating the Influences of the Adsorbed Species on Catalytic Activity for Hydrogen Oxidation Reaction in Alkaline Electrolyte. *J. Am. Chem. Soc.* **2017**, *139*, 5156–5163.
- (14) Sheng, W.; Myint, M.; Chen, J. G.; Yan, Y. Correlating the Hydrogen Evolution Reaction Activity in Alkaline Electrolytes with the Hydrogen Binding Energy on Monometallic Surfaces. *Energy Environ. Sci.* **2013**, *6*, 1509–1512.
- (15) Wang, Y.; Wang, G.; Li, G.; Huang, B.; Pan, J.; Liu, Q.; Han, J.; Xiao, L.; Lu, J.; Zhuang, L. Pt–Ru Catalyzed Hydrogen Oxidation in Alkaline Media: Oxophilic Effect or Electronic Effect? *Energy Environ. Sci.* **2015**, *8*, 177–181.
- (16) Strmcnik, D.; Uchimura, M.; Wang, C.; Subbaraman, R.; Danilovic, N.; van der Vliet, D.; Paulikas, A. P.; Stamenkovic, V. R.; Markovic, N. M. Improving the Hydrogen Oxidation Reaction Rate by Promotion of Hydroxyl Adsorption. *Nat. Chem.* **2013**, *5*, 300–306.
- (17) Subbaraman, R.; Tripkovic, D.; Strmcnik, D.; Chang, K.; Uchimura, M.; Paulikas, A. P.; Stamenkovic, V.; Markovic, N. M.

- Enhancing Hydrogen Evolution Activity in Water Splitting by Tailoring  $\text{Li}^+\text{-Ni(OH)}_2\text{-Pt}$  Interfaces. *Science* **2011**, *334*, 1256–1260.
- (18) Zeng, Z.; Chang, K.-C.; Kubal, J.; Markovic, N. M.; Greeley, J. Stabilization of Ultrathin (Hydroxy)Oxide Films on Transition Metal Substrates for Electrochemical Energy Conversion. *Nat. Energy* **2017**, *2*, 17070.
- (19) Huang, T.; Shen, T.; Gong, M.; Deng, S.; Lai, C.; Liu, X.; Zhao, T.; Teng, L.; Wang, D. Ultrafine Ni-B Nanoparticles for Efficient Hydrogen Evolution Reaction. *Chin. J. Catal.* **2019**, *40*, 1867–1873.
- (20) Huang, L.; Zou, Y.; Chen, D.; Wang, S. Electronic Structure Regulation on Layered Double Hydroxides for Oxygen Evolution Reaction. *Chin. J. Catal.* **2019**, *40*, 1822–1840.
- (21) Ni, W.; Krammer, A.; Hsu, C.-S.; Chen, H. M.; Schueler, A.; Hu, X.  $\text{Ni}_3\text{N}$  as an Active Hydrogen Oxidation Reaction Catalyst in Alkaline Medium. *Angew. Chem., Int. Ed.* **2019**, *58*, 7445–7449.
- (22) Wang, M.; Yang, H.; Shi, J.; Chen, Y.; Zhou, Y.; Wang, L.; Di, S.; Zhao, X.; Zhong, J.; Cheng, T.; et al. Alloying Nickel with Molybdenum Significantly Accelerates Alkaline Hydrogen Electrocatalysis. *Angew. Chem., Int. Ed.* **2021**, *60*, 5771–5777.
- (23) Tan, T. L.; Wang, L.-L.; Zhang, J.; Johnson, D. D.; Bai, K. Platinum Nanoparticle During Electrochemical Hydrogen Evolution: Adsorbate Distribution, Active Reaction Species, and Size Effect. *ACS Catal.* **2015**, *5*, 2376–2383.
- (24) Xie, C.; Niu, Z.; Kim, D.; Li, M.; Yang, P. Surface and Interface Control in Nanoparticle Catalysis. *Chem. Rev.* **2020**, *120*, 1184–1249.
- (25) Hamo, E. R.; Singh, R. K.; Douglin, J. C.; Chen, S.; Hassine, M. B.; Carbo-Argibay, E.; Lu, S.; Wang, H.; Ferreira, P. J.; Rosen, B. A.; et al. Carbide-Supported PtRu Catalysts for Hydrogen Oxidation Reaction in Alkaline Electrolyte. *ACS Catal.* **2021**, *11*, 932–947.
- (26) Zadick, A.; Dubau, L.; Sergent, N.; Berthomé, G.; Chatenet, M. Huge Instability of Pt/C Catalysts in Alkaline Medium. *ACS Catal.* **2015**, *5*, 4819–4824.
- (27) Zhong, Y.; Xia, X.; Shi, F.; Zhan, J.; Tu, J.; Fan, H. J. Transition Metal Carbides and Nitrides in Energy Storage and Conversion. *Adv. Sci.* **2016**, *3*, 1500286.
- (28) Tian, X.; Luo, J.; Nan, H.; Zou, H.; Chen, R.; Shu, T.; Li, X.; Li, Y.; Song, H.; Liao, S.; et al. Transition Metal Nitride Coated with Atomic Layers of Pt as a Low-Cost, Highly Stable Electrocatalyst for the Oxygen Reduction Reaction. *J. Am. Chem. Soc.* **2016**, *138*, 1575–1583.
- (29) Garg, A.; Gonçalves, D. S.; Liu, Y.; Wang, Z.; Wang, L.; Yoo, J. S.; Kolpak, A.; Rioux, R. M.; Zanchet, D.; Román-Leshkov, Y. Impact of Transition Metal Carbide and Nitride Supports on the Electronic Structure of Thin Platinum Overlayers. *ACS Catal.* **2019**, *9*, 7090–7098.
- (30) Guo, Y.; Tang, J.; Henzie, J.; Jiang, B.; Qian, H.; Wang, Z.; Tan, H.; Bando, Y.; Yamauchi, Y. Assembly of Hollow Mesoporous Nanoarchitectures Composed of Ultrafine  $\text{Mo}_2\text{C}$  Nanoparticles on N-doped Carbon Nanosheets for Efficient Electrocatalytic Reduction of Oxygen. *Mater. Horiz.* **2017**, *4*, 1171–1177.
- (31) Coskun, H.; Aljabour, A.; de Luna, P.; Sun, H.; Nishiumi, N.; Yoshida, T.; Koller, G.; Ramsey, M. G.; Greunz, T.; Stifter, D.; et al. Metal-Free Hydrogen-Bonded Polymers Mimic Noble Metal Electrocatalysts. *Adv. Mater.* **2020**, *32*, 1902177.
- (32) Wang, Z.; Xu, X.; Liu, Z.; Ji, S.; Ahmed Idris, S. O.; Liu, J. Hollow Spheres of  $\text{Mo}_2\text{C}@C$  as Synergistically Confining Sulfur Host for Superior Li–S Battery Cathode. *Electrochim. Acta* **2020**, *332*, 135482.
- (33) Wang, C.; Sun, Y.; Tian, E.; Fu, D.; Zhang, M.; Zhao, X.; Ye, W. Easy Access to Trace-Loading of Pt on Inert  $\text{Ni}_3\text{N}$  Nanoparticles with Significantly Improved Hydrogen Evolution Activity at Entire pH Values. *Electrochim. Acta* **2019**, *320*, 134597.
- (34) Yan, G.; Feng, X.; Khan, S. U.; Xiao, L.; Xi, W.; Tan, H.; Ma, Y.; Zhang, L.; Li, Y. Polyoxometalate and Resin-Derived P-Doped  $\text{Mo}_2\text{C}@N$ -Doped Carbon as a Highly Efficient Hydrogen-Evolution Reaction Catalyst at All pH Values. *Chem. Asian. J.* **2018**, *13*, 158–163.
- (35) Chen, M.; Qi, J.; Guo, D.; Lei, H.; Zhang, W.; Cao, R. Facile Synthesis of Sponge-like  $\text{Ni}_3\text{N}/\text{NC}$  for Electrocatalytic Water Oxidation. *Chem. Commun.* **2017**, *53*, 9566–9569.
- (36) Guo, M.; Xu, M.; Qu, Y.; Hu, C.; Yan, P.; Isimjan, T. T.; Yang, X. Electronic/Mass Transport Increased Hollow Porous  $\text{Cu}_3\text{P}/\text{MoP}$  Nanospheres with Strong Electronic Interaction for Promoting Oxygen Reduction in Zn-Air Batteries. *Appl. Catal. B: Environ.* **2021**, *297*, 120415.
- (37) Gao, Z.; Fan, G.; Liu, M.; Yang, L.; Li, F. Dandelion-like Cobalt Oxide Microsphere-Supported RuCo Bimetallic Catalyst for Highly Efficient Hydrogenolysis of 5-Hydroxymethylfurfural. *Appl. Catal. B: Environ.* **2018**, *237*, 649–659.
- (38) Yu, B.; Huang, A.; Chen, D.; Srinivas, K.; Zhang, X.; Wang, X.; Wang, B.; Ma, F.; Liu, C.; Zhang, W.; et al. In Situ Construction of  $\text{Mo}_2\text{C}$  Quantum Dots-Decorated CNT Networks as a Multifunctional Electrocatalyst for Advanced Lithium–Sulfur Batteries. *Small* **2021**, *17*, 2100460.
- (39) Cui, C.; Cheng, R.; Zhang, H.; Zhang, C.; Ma, Y.; Shi, C.; Fan, B.; Wang, H.; Wang, X. Ultrastable MXene@Pt/SWCNTs' Nanocatalysts for Hydrogen Evolution Reaction. *Adv. Funct. Mater.* **2020**, *30*, 2000693.
- (40) Wei, H.; Wang, J.; Lin, Q.; Zou, Y.; Chen, X. a.; Zhao, H.; Li, J.; Jin, H.; Lei, Y.; Wang, S. Incorporating Ultra-Small N-doped  $\text{Mo}_2\text{C}$  Nanoparticles onto 3D N-Doped Flower-like Carbon Nanospheres for Robust Electrocatalytic Hydrogen Evolution. *Nano Energy* **2021**, *86*, 106047.
- (41) Jeong, H.-Y.; Kim, D.-g.; Akpe, S. G.; Paidi, V. K.; Park, H. S.; Lee, S.-H.; Lee, K.-S.; Ham, H. C.; Kim, P.; Yoo, S. J. Hydrogen-Mediated Thin Pt Layer Formation on  $\text{Ni}_3\text{N}$  Nanoparticles for the Oxygen Reduction Reaction. *ACS Appl. Mater. Interfaces* **2021**, *13*, 24624–24633.
- (42) Pei, Y.; Rezaei, B.; Zhang, X.; Li, Z.; Shen, H.; Yang, M.; Wang, J. Interface Catalysis by Pt Nanocluster@ $\text{Ni}_3\text{N}$  for Bifunctional Hydrogen Evolution and Oxygen Evolution. *Mater. Chem. Front.* **2020**, *4*, 2665–2672.
- (43) Li, M.; Zhu, Y.; Wang, H.; Wang, C.; Pinna, N.; Lu, X. Ni Strongly Coupled with  $\text{Mo}_2\text{C}$  Encapsulated in Nitrogen-Doped Carbon Nanofibers as Robust Bifunctional Catalyst for Overall Water Splitting. *Adv. Energy Mater.* **2019**, *9*, 1803185.
- (44) Liu, Y.; Zhang, J.; Li, Y.; Qian, Q.; Li, Z.; Zhang, G. Realizing the Synergy of Interface Engineering and Chemical Substitution for  $\text{Ni}_3\text{N}$  Enables its Bifunctionality Toward Hydrazine Oxidation Assisted Energy-Saving Hydrogen Production. *Adv. Funct. Mater.* **2021**, *31*, 2103673.
- (45) Chen, Y.; Yu, J.; Jia, J.; Liu, F.; Zhang, Y.; Xiong, G.; Zhang, R.; Yang, R.; Sun, D.; Liu, H.; et al. Metallic  $\text{Ni}_3\text{Mo}_3\text{N}$  Porous Microrods with Abundant Catalytic Sites as Efficient Electrocatalyst for Large Current Density and Superstability of Hydrogen Evolution Reaction and Water Splitting. *Appl. Catal. B: Environ.* **2020**, *272*, 118956.
- (46) Zhao, T.; Hu, Y.; Gong, M.; Lin, R.; Deng, S.; Lu, Y.; Liu, X.; Chen, Y.; Shen, T.; Hu, Y.; et al. Electronic Structure and Oxophilicity Optimization of Mono-layer Pt for Efficient Electrocatalysis. *Nano Energy* **2020**, *74*, 104877.
- (47) Yang, Y.; Shao, X.; Zhou, S.; Yan, P.; Isimjan, T. T.; Yang, X. Interfacial Electronic Coupling of  $\text{NC}@W\text{O}_3\text{-W}_2\text{C}$  Decorated Ru Clusters as a Reversible Catalyst toward Electrocatalytic Hydrogen Oxidation and Evolution Reactions. *ChemSusChem* **2021**, *14*, 2992–3000.
- (48) Qin, B.; Yu, H.; Gao, X.; Yao, D.; Sun, X.; Song, W.; Yi, B.; Shao, Z. Ultrathin IrRu Nanowire Networks with High Performance and Durability for the Hydrogen Oxidation Reaction in Alkaline Anion Exchange Membrane Fuel Cells. *J. Mater. Chem. A* **2018**, *6*, 20374–20382.
- (49) Duan, Y.; Yu, Z.-Y.; Yang, L.; Zheng, L.-R.; Zhang, C.-T.; Yang, X.-T.; Gao, F.-Y.; Zhang, X.-L.; Yu, X.; Liu, R.; et al. Bimetallic Nickel-Molybdenum/Tungsten Nanoalloys for High-efficiency Hydrogen Oxidation Catalysis in Alkaline Electrolytes. *Nat. Commun.* **2020**, *11*, 4789.

(50) Zhuang, Z.; Giles, S. A.; Zheng, J.; Jenness, G. R.; Caratzoulas, S.; Vlachos, D. G.; Yan, Y. Nickel Supported on Nitrogen-Doped Carbon Nanotubes as Hydrogen Oxidation Reaction Catalyst in Alkaline Electrolyte. *Nat. Commun.* **2016**, *7*, 10141.

(51) Yang, Y.; Sun, X.; Han, G.; Liu, X.; Zhang, X.; Sun, Y.; Zhang, M.; Cao, Z.; Sun, Y. Enhanced Electrocatalytic Hydrogen Oxidation on Ni/NiO/C Derived from a Nickel-Based Metal–Organic Framework. *Angew. Chem., Int. Ed.* **2019**, *58*, 10644–10649.

(52) Ma, Z.; Chen, C.; Cui, X.; Zeng, L.; Wang, L.; Jiang, W.; Shi, J. Hydrogen Evolution/Oxidation Electrocatalysts by the Self-Activation of Amorphous Platinum. *ACS Appl. Mater. Interfaces* **2021**, *13*, 44224–44233.

(53) Hu, Y.; Yu, H.; Qi, L.; Dong, J.; Yan, P.; Taylor Isimjan, T.; Yang, X. Interface Engineering of Needle-like P-Doped MoS<sub>2</sub>/CoP Arrays as Highly Active and Durable Bifunctional Electrocatalyst for Overall Water Splitting. *ChemSusChem* **2021**, *14*, 1565–1573.

(54) Li, Z.; Feng, Y.; Liang, Y.-L.; Cheng, C.-Q.; Dong, C.-K.; Liu, H.; Du, X.-W. Stable Rhodium (IV) Oxide for Alkaline Hydrogen Evolution Reaction. *Adv. Mater.* **2020**, *32*, 1908521.

(55) Kundu, M. K.; Mishra, R.; Bhowmik, T.; Barman, S. Rhodium Metal–Rhodium Oxide (Rh–Rh<sub>2</sub>O<sub>3</sub>) Nanostructures with Pt-like or Better Activity towards Hydrogen Evolution and Oxidation Reactions (HER, HOR) in Acid and Base: Correlating its HOR/HER Activity with Hydrogen Binding Energy and Oxophilicity of the Catalyst. *J. Mater. Chem. A* **2018**, *6*, 23531–23541.

(56) Su, L.; Gong, D.; Yao, N.; Li, Y.; Li, Z.; Luo, W. Modification of the Intermediate Binding Energies on Ni/Ni<sub>3</sub>N Heterostructure for Enhanced Alkaline Hydrogen Oxidation Reaction. *Adv. Funct. Mater.* **2021**, *31*, 2106156.

(57) Zhang, B.; Zhao, G.; Zhang, B.; Xia, L.; Jiang, Y.; Ma, T.; Gao, M.; Sun, W.; Pan, H. Lattice-Confined Ir Clusters on Pd Nanosheets with Charge Redistribution for the Hydrogen Oxidation Reaction under Alkaline Conditions. *Adv. Mater.* **2021**, *33*, 2105400.

(58) Chen, Y. W.; Prange, J. D.; Dühnen, S.; Park, Y.; Gunji, M.; Chidsey, C. E. D.; McIntyre, P. C. Atomic Layer-Deposited Tunnel Oxide Stabilizes Silicon Photoanodes for Water Oxidation. *Nat. Mater.* **2011**, *10*, 539–544.

(59) Song, F.; Li, W.; Yang, J.; Han, G.; Yan, T.; Liu, X.; Rao, Y.; Liao, P.; Cao, Z.; Sun, Y. Interfacial Sites between Cobalt Nitride and Cobalt Act as Bifunctional Catalysts for Hydrogen Electrochemistry. *ACS Energy Lett.* **2019**, *4*, 1594–1601.